metals

Article

Impact of a Transient and Asymmetrical Distribution of the Electric Arc on the Solidification Conditions of the Ingot in the VAR Process

Pierre-Olivier Delzant [1], Pierre Chapelle [1,*], Alain Jardy [1], Alexey Matveichev [2] and Yvon Millet [3]

[1] Institut Jean Lamour, UMR 7198 CNRS, Université de Lorraine, LabEx DAMAS, BP 50840, 54011 Nancy CEDEX, France; pierre-olivier.delzant@hotmail.fr (P.-O.D.); alain.jardy@univ-lorraine.fr (A.J.)
[2] O2M Solutions, 2 Allée André Guinier, 54000 Nancy, France; alexey@o2m.solutions
[3] TIMET Savoie, Avenue Paul Girod, 73400 Ugine, France; yvon.millet@timet.com
* Correspondence: pierre.chapelle@univ-lorraine.fr; Tel.: +33-37-274-2719

Abstract: Vacuum Arc Remelting is an important method of processing reactive and refractory liquid metal alloys, including titanium and zirconium alloys. Recent measurements of the electric arc dynamics under the presence of a time-varying magnetic field during an industrial melt of a Ti64 alloy provided evidence of the existence of an ensemble arc motion. Such motion is responsible for transient and non-axisymmetric inputs of electric current and energy at the top surface of the remelted ingot. The present work is an attempt to evaluate, using a simplified numerical simulation approach, to what extent the solidification conditions of the VAR ingot and, consequently, the quality of the final product, may be affected by this phenomenon. The reported results indicate that, under the worst case conditions, the relative vanadium segregation in the solidified ingot can reach values as high as 12.5%.

Keywords: vacuum arc remelting; titanium alloy; electric arc; solidification

Citation: Delzant, P.-O.; Chapelle, P.; Jardy, A.; Matveichev, A.; Millet, Y. Impact of a Transient and Asymmetrical Distribution of the Electric Arc on the Solidification Conditions of the Ingot in the VAR Process. *Metals* **2022**, *12*, 500. https://doi.org/10.3390/met12030500

Academic Editor: Noé Cheung

Received: 8 February 2022
Accepted: 11 March 2022
Published: 16 March 2022

1. Introduction

The vacuum arc remelting (VAR) process is widely used for producing reactive and high melting temperature metals, such as Ti and Zr alloys, nickel base alloys and special steels. The process relies on the use of an electric arc to melt under vacuum a consumable electrode. Melting results in the creation of a thin liquid metal film at the electrode tip, which drips through the arc to create an ingot that progressively builds up within a water-cooled copper crucible (Figure 1).

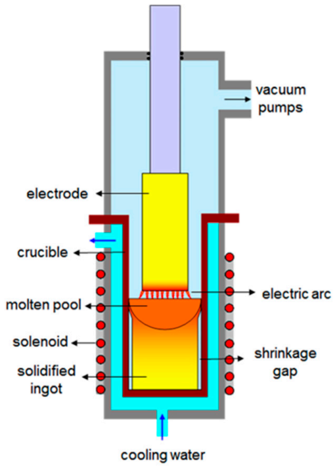

Figure 1. Schematic of the VAR process (Reproduced from [1], with permission from Elsevier, 2022).

This process enables the production of ingots with reduced impurity content and segregation as well as a controlled microstructure. Note that for the melt of specific alloys (e.g., Ti and Zr alloys) an external axial magnetic field is used to confine the arc under the electrode and to promote stirring and homogenization of the metal in the liquid pool present at the ingot top. Among the process conditions, the characteristics of the arc play a crucial role in the operation and performance of the process. They determine the spatio-temporal distributions of the current and thermal energy inputs at the top of the ingot, which both affect, through controlling the hydrodynamics and the thermal field of the liquid metal, the ingot solidification conditions and, thus, its final quality [2].

Despite the central importance of the electric arc in the process, the characteristics and the role of the arc have been little investigated in the literature. The experimental study of the electric arc in a VAR furnace is indeed extremely challenging due to the furnace configuration (with no direct visual access to the arc) and the hostile conditions (high temperature and low-pressure conditions) inside the furnace. Consequently, the knowledge regarding the arc behavior is very scarce.

At small time scales (less than a few milliseconds), it has been established due to direct visualization experiments performed in specifically instrumented furnace that the arc consists of multiple tiny cathode spots producing a diffuse metal vapor plasma that enables the electrical current transfer between the electrode and the ingot, each spot carrying a current of the order of 100 A [3–5]. Due to the fast motion of the cathode spots over the whole electrode surface, such an arc behavior was thought to provide a macro-uniform heat and electrical input at the ingot top [6].

This latter conclusion was however put under questions by several studies performed on industrial VAR furnaces, which succeeded to infer unexpected results on the spatio-temporal-distribution of the arc at large time scales. These latter studies relied either on magnetic flux measurements outside the furnace or optical techniques. Magnetic flux measurements revealed that the arc centroid was most of the time off-centered and rotated around the electrode centerline with a time period of approximately 20–40 s during VAR of Inconel 718 [7] and 1–20 s during VAR of a Ti64 alloy [8]. More recently, using an optical technique inspired from that proposed by Aikin and Williamson [9], we reported similar results during VAR of a Ti64 alloy showing the existence of an asymmetrical arc distribution with a periodic ensemble arc motion leading to various arc patterns [1].

As far as the modelling of the VAR process is concerned, several models have been reported in the literature that focused on various aspects of the process, mostly dealing with the growth and solidification of the ingot (e.g., [10–16]). The technique usually applied to simulate the ingot is based on a Computational Fluid Dynamics (CFD) approach.

The basic content of these models includes a simulation of the hydrodynamic and thermal behavior of the metal within the melt pool coupled to some fairly basic description of the solidification of the metal. The complexity of the models varies depending on the integration of various additional physical phenomena, such as the turbulence phenomena, the electromagnetic stirring forces and the solute transport. A refinement of these models is their coupling with mesoscopic (or microscopic depending on the scale) models aimed at simulating dendritic solidification in more detail [11,13].

Most of these models consider an axisymmetric 2D geometry and, therefore, do not enable to consider a non-axisymmetric distribution and ensemble motion of the arc at the top of the ingot, as mentioned previously. An attempt to consider such a phenomenon was made by Pericleous et al. in developing a full three-dimensional model [14]. Their study indicated that the presence of a moving and off-center electric arc has an impact on the metal flow within the melt pool, the temperature field of the ingot as well as the current distribution in the furnace.

The objective of this work is to investigate the influence of an asymmetrical distribution and ensemble motion of the arc on the ingot evolution. The rest of the manuscript is organized as follows. Section 2 presents various arc patterns that were observed during VAR of a Ti64 alloy. In Section 3, a simple procedure is described to simulate these patterns and to calculate the resulting distributions of energy and current across the top surface of the ingot. These distributions are then incorporated as boundary conditions into a 3D model of the ingot evolution. In Section 4, we present various typical simulation results illustrating the impacts on the melt pool and solidification conditions of the ingot caused by an asymmetric arc motion.

2. Experimental Evidence of the Existence of a Time Varying Asymmetrical Arc Distribution

A detailed description of the experimental work can be found in [1]. Here, we only give a brief summary of the main results needed for the understanding of the modelling work presented in the rest of the paper.

2.1. Experimental Methodology

Given the configuration of a VAR furnace, it is not possible to directly observe the light emitted by the arc during a melt. Only the light reflected by the surface of the molten pool and transmitted through the annulus between the electrode and the crucible wall toward the top of the furnace may be analyzed. In the present work, the intensity of this reflected light was monitored by a set of photodiodes located inside the furnace (Figure 2). The analysis of the variations of the light intensity recorded simultaneously in various regions of the annulus gap was then used to infer useful information about the arc dynamics. In particular, it was possible to calculate the position of the arc luminosity centroid at any time and follow its motion as a function of time.

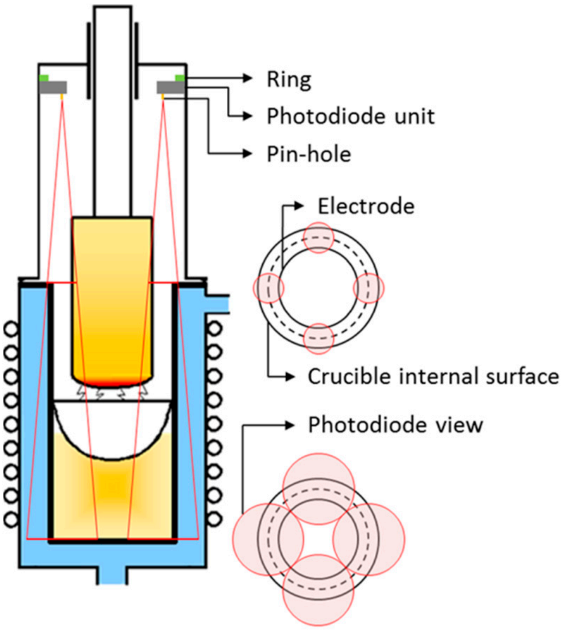

Figure 2. Schematic of the installation of the photodiode instrumentation inside a VAR furnace (Reproduced from [1], with permission from Elsevier, 2022).

The reflected light intensity data were recorded using four photodiodes PDA36A (Thorlabs Inc., Newton, NJ, USA) installed inside a full-scale production VAR furnace (Retech, Ukiah, CA, USA) on top of the vacuum chamber. The photodiodes were equipped with interferential filters to remove contributions due to thermal radiation of the molten pool and with pinholes designed to limit the photodiode vision field and prevent any overlapping of the vision fields of the photodiodes throughout the entire melt. The recorded photodiode signals were calibrated with the hypothesis that the average arc luminosity under each photodiode is identical during the melt plateau. The position of the arc luminosity centroid at every instant was then derived from the calibrated signals using the following formula:

$$x_g = \sum(x_i V_i) / \sum V_i \text{ and } y_g = \sum(y_i V_i) / \sum V_i \tag{1}$$

where (x_i, y_i) is the position of photodiode i, which delivers the voltage V_i.

Measurements were made during the melt of a 5 ton Ti64 electrode. The melt was operated with an imposed external axial magnetic field, whose magnitude followed a time varying periodic sequence (called the stirring sequence). For confidentiality reasons, the melt parameters cannot be given. Therefore, arbitrary units are used.

2.2. *Spatio-Temporal Distribution of the Arc Luminosity Centroid*

The measurements revealed the existence, most of the time, of an asymmetric distribution of the arc evolving in a periodic way and giving rise to various repetitive overall motions of the arc luminosity centroid (which we called patterns). During the melt reported here, three regular arc patterns were observed (referred hereafter as patterns A, B and C). A typical trajectory of the arc centroid throughout a single stirring period during these three patterns is given in Figure 3. A color code defined in Figure 3d is used to identify the different stages of the stirring sequence.

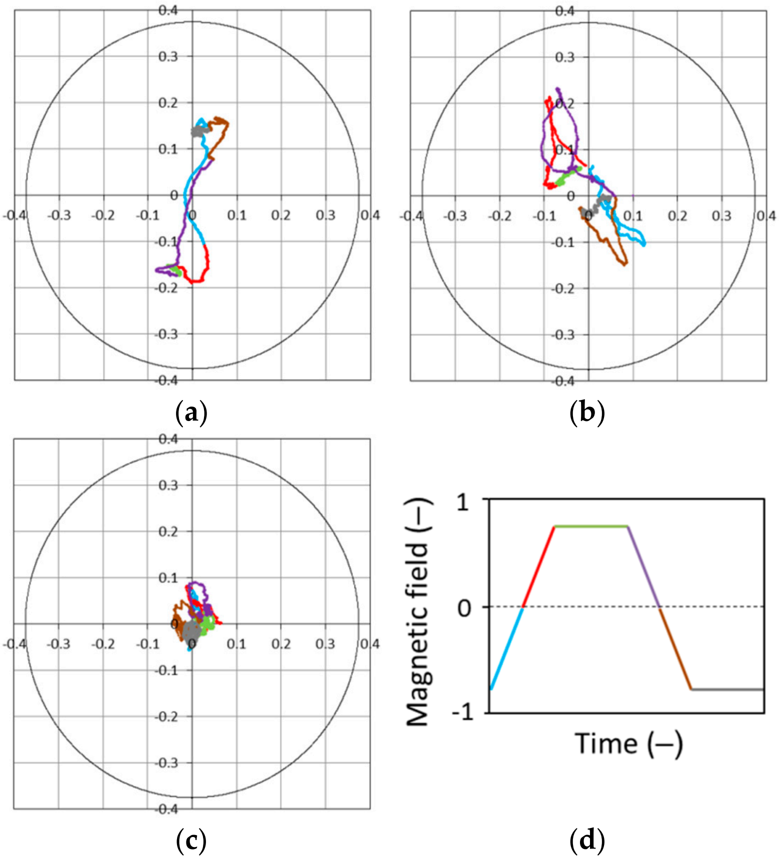

Figure 3. Typical trajectory of the arc centroid during a single stirring period: (**a**) pattern A, (**b**) pattern B, (**c**) pattern C and (**d**) color code of the precise moment in the stirring sequence. (Reproduced from [1], with permission from Elsevier, 2022).

The first two patterns (A and B) were highly correlated with the stirring sequence. The arc centroid is animated by a back-and-forth movement between two off-center and almost diametrically opposite regions, which are characterized by a higher stability. The movement is quite linear in the case of pattern A and elliptical in the case of pattern B. The motion of the arc centroid occurs during phases of magnetic field polarity reversal (stirring ramp), while the phases of constant magnetic field (stirring plateau) correspond to a relative stability of the centroid in one of the two off-center regions. The centroid motion occurs mostly during the first half of the stirring ramp, i.e., when the strength of the magnetic field decreases.

Moreover, the centroid tends to move towards a position further off-center before locating in a stable region. Each stable region is associated with a given polarity of the stirring current. The pattern C was observed only during the final stage of the melt (i.e., hot-topping) and is significantly different from patterns A and B. During this pattern, the arc centroid was always located a very small distance from the electrode center line and its angular position experienced much greater variations than in previous patterns. However, the stirring plateaus remain phases where the position of the centroid was generally more stable.

3. Modelling

This section describes a first approach to consider, in a simulation of the evolution of a VAR ingot, the various dynamic behaviors of the arc observed in the above experimental work. Due to the strong temporal variability of the observed arc patterns, it is not conceivable to incorporate directly into the ingot simulation software the recorded position data of the arc centroid. Therefore, as a preliminary step, a simplified representation (i.e., model) of these patterns was derived.

Then, the time-dependent spatial distributions of power and current density brought by the arc pattern at the top surface of the ingot were calculated from this model and used eventually as boundary conditions in the ingot model. Because of the asymmetric nature of the patterns described by the arc, a 3D model of the ingot was necessary. The dedicated simulation software RAVEL (version 2, CNRS, Nancy, France) describing the ingot growth and solidification, recently developed at Institut Jean Lamour, was adopted in the present work.

3.1. Modelling of the Arc Patterns

The modelling of the observed arc patterns is based on the idea that it is possible to represent complex patterns as a combination of elementary distributions with simple dynamics. Three individual elementary distributions were introduced (Figure 4): namely, an immobile and uniform distribution covering the entire ingot top surface (hereafter referred as "arc component U"), a distribution of disc shape with a linear translational motion (hereafter referred as "arc component T") and a distribution of disc shape with a rotational motion (hereafter referred as "arc component R").

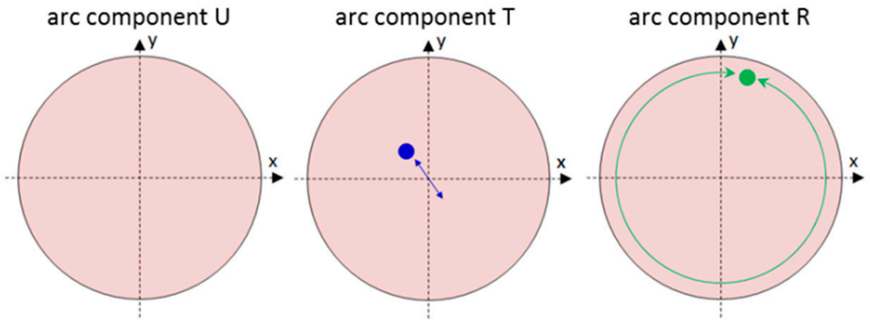

Figure 4. Schematic of the three individual elementary arc distributions.

The two main patterns (A and B) identified in the experimental work may be represented as a combination of the dynamics of two or three of these elementary distributions. Pattern A may be described as resulting of a combination of the arc components U and T, while pattern B may be described as resulting of a combination of the arc components U, T and R. Each elementary distribution is characterized by a set of parameters that need to be defined as input data: the fraction of the total arc current carried by the elementary distribution, its shape and spatial extent and the trajectory that it follows. In the following, we detail, as an illustrative example, the parameters set to model the pattern B.

Figure 5 shows the adjusted temporal evolution of the x-coordinate of the arc component T during a stirring period. By definition, the y-coordinate of the arc component T remains equal to zero. In accordance with the experimental observations, the motion of the arc component takes place only during the stirring ramps.

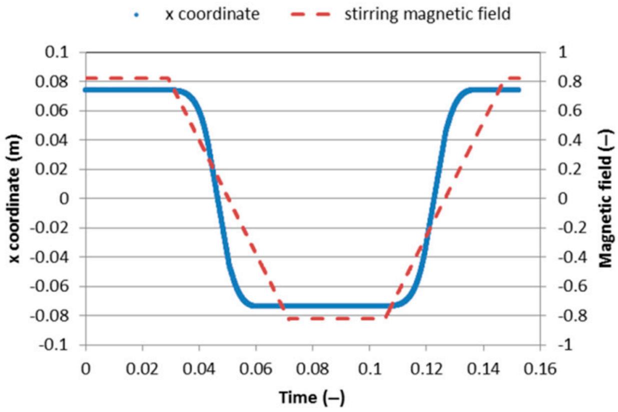

Figure 5. Time evolution during a stirring period of the x-coordinate of the arc component T.

As far as the arc component R is concerned, its radial coordinate was set to a significant off-center position (0.25 m) corresponding to about 2/3 of the ingot radius, while its azimuthal coordinate was considered to follow during a stirring period the temporal evolution presented in Figure 6. Note that the arc component R is left the possibility to rotate with a constant angular velocity during the stirring plateaus. This choice was made in order to be consistent with results of the literature indicating that the arc may adopt a rotational motion under the application of a constant axial magnetic field [17].

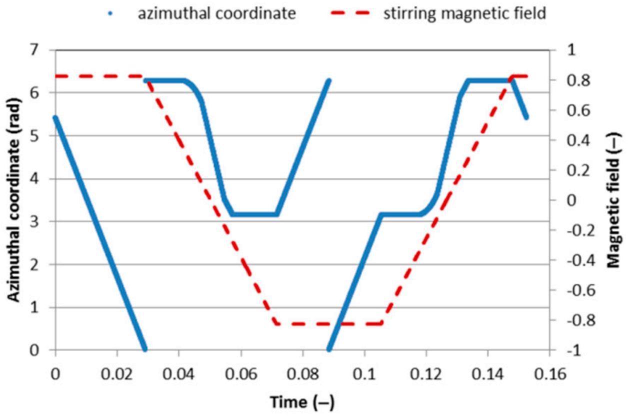

Figure 6. Time evolution during a stirring period of the azimuthal coordinate of the arc component R.

The adjusted values of the current fraction carried by the arc components U, T and R, which best reproduce the B pattern, are presented in Figure 7. The current fraction of the U component is assumed to be constant for reasons of simplicity and that of the arc component R is zero during the stirring plateau, due to the stability of the arc observed during this time interval. On the other hand, the radius of the U, T and R components were kept constant throughout the whole stirring sequence and set respectively to 0.415 m (ingot radius), 0.15 and 0.10 m. In addition, the current density and the power carried by each arc component were considered to be uniform.

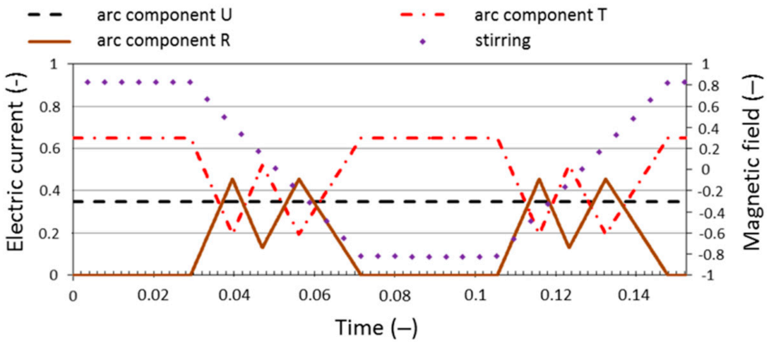

Figure 7. Time evolution during a stirring period of the currents carried by the arc components U, T and R.

All of this data allowed us to define the power and current density distributions produced by each arc component at the top of the ingot that may be used as boundary conditions in the RAVEL software. Figure 8 compares the trajectory of the arc centroid during half of a stirring period obtained experimentally (in blue) to that simulated from the present model (in green) using the input data detailed above.

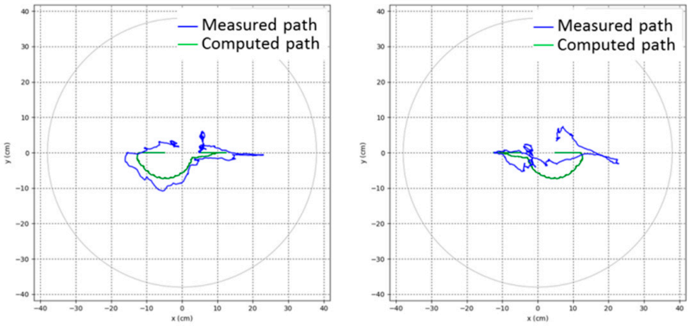

Figure 8. Comparison during two consecutive half stirring periods of the measured and computed paths of the electric arc centroid.

Overall, there is satisfactory agreement between both trajectories, which validates our modelling approach. The best agreement between the experimental and modeled trajectories in the first half of the stirring period (left figure) compared to that in the second half of the stirring period (right figure) may be explained by the fact that the parameters of arc components T and R were adjusted using the data from the first half of the stirring period.

3.2. 3D Model of the VAR Ingot

It is not the purpose of this paper to detail the simulation software RAVEL (Remelting using plasma Arc, Vacuum arc or ELectron beam). Such a description will be the subject of a future publication. Essentially, RAVEL is a 3D extension of the axisymmetric simulation code SOLAR, which has been developed at IJL during the last 25 years and extensively validated and used by several industrial partners [12,18–21].

Implemented using OpenFOAM® [22], the 3D solver code accounts for all the main physical phenomena addressed in 2D VAR simulation CFD codes, such as SOLAR. A non-exhaustive list of these phenomena is given below:

- Electric current distribution at any time at the ingot top, current flow within the ingot, electromagnetic forces related to the interaction between the melting current and both the self-induced and external axial magnetic fields.
- Arc power distribution at any time at the ingot top, heat content of the falling drops, convective-diffusive heat transfer within the ingot, dissipation of solidification latent

heat, ingot cooling through top surface radiation and water-cooling at the lateral and bottom surfaces.

- Solute content of the falling drops, convective transport of solute elements within the melt pool and mushy zone, evaporation of volatile elements at the pool surface, solute redistribution at the solid–liquid interface (hence solidification-induced segregation).
- Buoyancy caused by temperature and concentration gradients, forced convection due to the electromagnetic forces, turbulence of the flow in the pool, Darcy-like interaction between the solid and liquid within the mushy zone.
- Side wall heat transfer.

A previous version of the software was used to compute the coupled fluid flow and heat transfer in the liquid bath created by the Electron Beam melting of titanium in a hemispherical crucible and then to simulate dissolution experiments based on the immersion of refractory samples into the bath [21]. The 3D modelling of the continuous growth and solidification of a remelted ingot represents a following step.

4. Simulation Results and Discussion

As an example, we present the results of a simulation of the growth and solidification of a Ti64 ingot in the case where the arc describes during the entire remelting the pattern B. The full melt of a 750 mm diameter Ti64 electrode into an 830 mm diameter crucible was simulated using the RAVEL software. During the entire melt, we considered that the arc moved over the ingot top surface following the idealized B pattern as computed in the previous section. Note that, for the purpose of the present simulation, the pattern was kept constant throughout the full melt. The thermophysical properties of the Ti64 alloy required for the melt simulation were taken from Valencia and Quested [23], except for the emissivity, which was taken from Boivineau et al. [24]. The computational mesh consisted of hexahedral cells with an average height of 1.2 cm and average horizontal dimensions of 2.5 cm.

Figures 9 and 10 show, at two different time instants close to the end of the melt, the fields of current density, metal temperature and metal velocity in the mesh layer adjacent to the top surface of the ingot. Figure 9 refers to a time instant at the end of a negative ramp of the stirring sequence, while Figure 10 refers to a time instant at the start of a positive plateau of the stirring sequence. The figures include also schematics indicating the orientation of the arc pattern with respect to the figure and the precise location of the arc centroid.

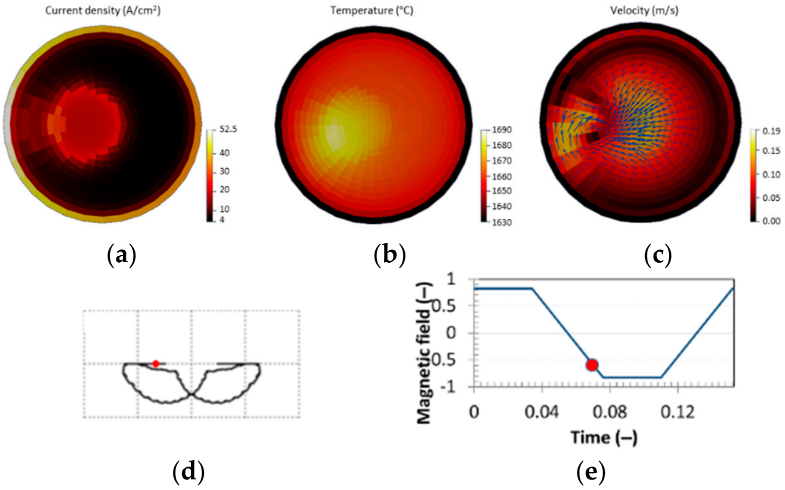

(**a**) (**b**) (**c**)

(**d**) (**e**)

Figure 9. Distributions of (**a**) the current density, (**b**) metal temperature and (**c**) liquid metal velocity in the mesh layer adjacent to the ingot top surface during a ramp of the stirring sequence. (**d**) Orientation of the arc pattern and actual location of the arc centroid. (**e**) Actual time instant along the stirring sequence.

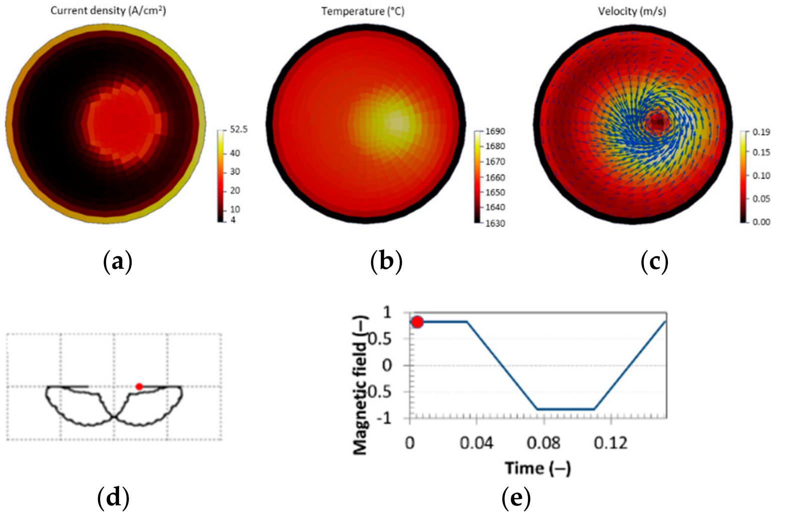

(**a**) (**b**) (**c**)

(**d**) (**e**)

Figure 10. Distributions of (**a**) the current density, (**b**) metal temperature and (**c**) liquid metal velocity in the mesh layer adjacent to the ingot top surface during a plateau of the stirring sequence. (**d**) Orientation of the arc pattern and actual location of the arc centroid. (**e**) Actual time instant along the stirring sequence.

A strong asymmetry of the distributions of the current density, temperature and velocity at the top of the ingot is observed in Figure 9. The maximum values of the metal temperature and metal velocity are 1685 °C and 13.6 cm/s, respectively. They are reached at significantly off-centered positions, located at 17.2 and 30.4 cm from the ingot centerline, respectively.

The asymmetries of the current density and temperature are the direct consequences of the asymmetries of the distributions of the current density and power, caused by the arc pattern and imposed as boundary conditions at the ingot top. The asymmetry of the flow of the metal in the molten pool is also a consequence of the asymmetries of the distributions of the current density and power at the ingot top. Indeed, the metal flow is governed by the buoyancy forces and Lorentz forces. Because of the asymmetries of the distributions of the current density and power at the ingot top, the distributions of these forces are strongly asymmetric. As observed in Figure 9, the metal flow in the molten pool is, thus, highly three dimensional.

Similarly to Figure 9, Figure 10 shows strong asymmetries of the current density, temperature and velocity distributions. The maximum values of the metal temperature and metal velocity (1685 °C and 18.3 cm/s, respectively) are comparable to those observed in Figure 9 but are located slightly closer to the ingot centerline (at a distance of 12 cm and 22.1, respectively) than in Figure 9. The comparison of Figures 9 and 10 shows a marked evolution of the distributions of the current density, temperature and velocity of the metal between the two time instants.

This evolution may be clearly correlated to the change in the arc centroid location, and its consequences on the distributions of the current density and power imposed as boundary conditions at the top of the ingot. In particular, the flow pattern of the metal at the ingot top is significantly different in Figures 9 and 10.

The vortex center is strongly off-centered, and the flow is mostly directed towards the centroid in Figure 9, while in Figure 10, the vortex center is closer to the ingot centerline and the velocity field presents some similarities with the flow that would be observed in the case of an axisymmetric arc distribution. Such a difference may be interpreted by considering the differences in the location and mobility of the arc centroid between the two time instants. Figure 9 refers indeed to a time instant when the arc was moving (stirring ramp), while Figure 10 refers to a time instant when the arc was mostly stable in a region close to the ingot centerline (stirring plateau).

Figures 11 and 12 show, at the same time instant considered in Figure 10 (i.e., during a plateau of the stirring sequence), the distributions of the temperature, liquid fraction and liquid metal velocity in two transverse sections ($y = 0$ and $x = 0$) of the ingot. As far as the temperature and the liquid fraction are concerned, a slight asymmetry in the fields of these two variables is observed in the section $x = 0$, while the fields of the two variables are fairly symmetrical in the section $y = 0$. In the section $x = 0$, the maximum depth of the molten pool is, thus, off-centered and located on the left half of the ingot at a distance of 7.6 cm from the ingot centerline. Moreover, the radius of the molten pool at mid-depth on the left half of the ingot is 17% higher than that on the right half.

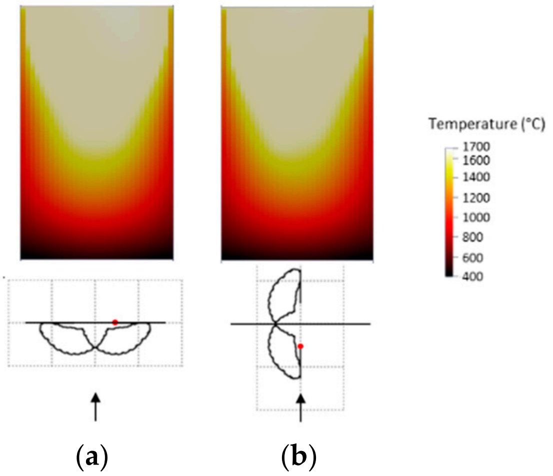

(**a**) (**b**)

Figure 11. Distributions of the metal temperature in two perpendicular transverse sections (**a**) $y = 0$ and (**b**) $x = 0$ of the ingot at the same time instant considered in Figure 10.

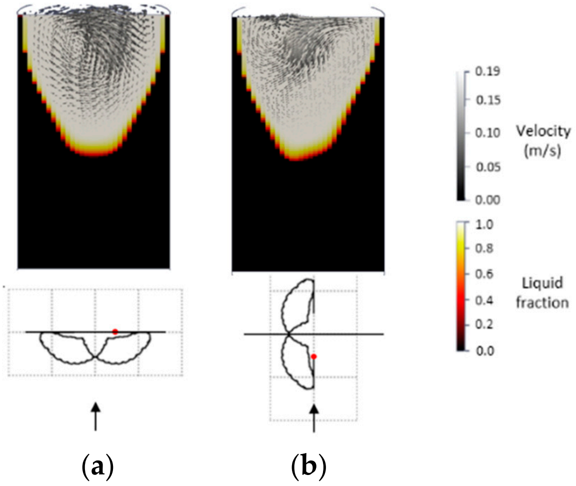

(**a**) (**b**)

Figure 12. Distributions of the liquid fraction and the velocity of the liquid metal in two perpendicular transverse sections (**a**) $y = 0$ and (**b**) $x = 0$ of the ingot at the same time instant considered in Figure 10.

Such an asymmetry effect in the section $x = 0$ is consistent with the fact that the section $x = 0$ is perpendicular to the pattern main orientation. The situation is different for the field of the liquid metal velocity, which exhibits a strong asymmetry in both sections ($x = 0$ and $y = 0$). In addition, the fields of the liquid metal velocity differ greatly in the two sections, revealing a complex three dimensional structure of the flow of liquid metal.

The distribution of the vanadium concentration in two transverse sections ($y = 0$ and $x = 0$) of the ingot at the same time instant considered in Figure 10 is plotted in Figure 13. The distribution of vanadium in the solidified region of the ingot is inhomogeneous.

Locally, the vanadium concentration reaches values as high as 4.5% (i.e., relative segregation of 12.5%), which differ greatly from the nominal concentration (4%), resulting in some significant segregation.

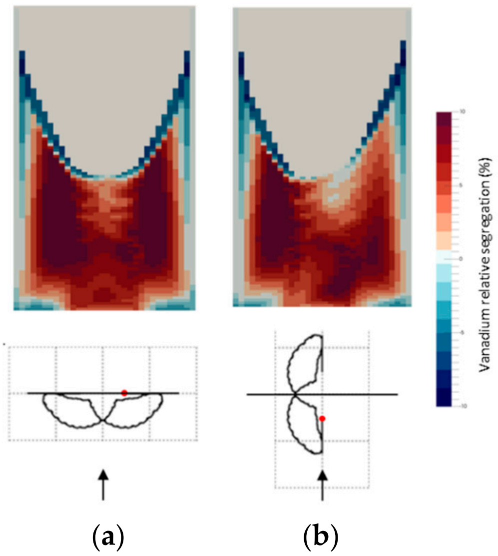

Figure 13. Distributions of vanadium relative segregation in the solidified part of the ingot. The results are shown in two perpendicular transverse sections (**a**) $y = 0$ and (**b**) $x = 0$ of the ingot at the same time instant considered in Figure 10.

Moreover, similarly to the observations made above for the temperature and liquid fraction distributions, the asymmetry of the arc distribution results in an asymmetry of the vanadium distribution, which is more pronounced in the section perpendicular to the main orientation of the pattern (i.e., $x = 0$). As observed in Figure 13, the overall vanadium enrichment is higher in the region of the ingot located underneath the arc pattern, i.e., in both the left and right halves of the ingot in the section $y = 0$ and only in the left half of the ingot in the section $x = 0$.

As a consequence, the segregation level is more severe in the section $y = 0$. The reasons for such a behavior remain unclear at present. This might be related to the local flow conditions close to the solidification front, resulting from the complex and constantly changing 3D flow patterns of the molten metal caused by the ensemble arc motion. A specific research study would be needed to identify precisely the underlying interaction mechanisms. One should recall here that the arc pattern was kept constant throughout the full melt. This certainly contributed to overestimating the impact of the pattern on the ingot (hence the high segregation level).

Indeed, the experimental study of the characteristics of pattern B revealed that the stable regions associated with the stirring plateaus move slowly during the melt [1], which should tend to lessen the impact of the pattern asymmetry on the ingot. Such effects on the vanadium concentration remain true for all alloy elements with a partition coefficient different from 1. Yet only results for vanadium are presented here for the sake of keeping the paper concise. If an influence of the asymmetric arc pattern on the temperature and liquid metal velocity was expected, one notes that the arc pattern also has a significant influence on the concentration of the alloying elements and therefore the segregation, hence the final quality of the ingot. This emphasizes the need to better understand and control the arc behavior during a VAR melt.

5. Conclusions

This paper describes our efforts to investigate the influence of transient and asymmetrical distributions of the energy and current density at the ingot top caused by an ensemble arc motion on the solidification conditions of a VAR ingot. The VAR melt of a Ti64 alloy electrode was simulated using the 3D dedicated software RAVEL, inside which a simplified representation of the pattern followed by the arc centroid at the ingot top surface, such as observed experimentally under the presence of a time-varying magnetic field, was implemented.

The simulation results indicated that the dynamic and thermal conditions in the molten pool were seriously influenced by the time and position dependent arc distribution, resulting in significant asymmetries and three-dimensional features as well as transient effects. The molten pool presented a larger volume in the part of the ingot underneath the arc pattern. As a result, the maximum depth of the molten pool was reached in the section perpendicular to the arc pattern main orientation at an off-centered position, located at a radial distance of about 20% of the ingot radius.

The arc ensemble motion also had a great impact on the distribution of the alloy element concentration, leading again to some asymmetries and eventually to a more severe segregation with some detrimental effects on the quality of the final ingot. Overall, the segregation was more important in the regions of the ingot located underneath the arc pattern. Under the worst-case conditions considered in the present paper, the maximum relative segregation in vanadium reached values as high as 12.5%.

Further studies, especially on the influence of the parameters of the applied external magnetic field (field intensity and alternating or continuous field) on the arc dynamics, are required in the future to uncover the underlying mechanisms governing the ensemble arc motion. These are a precondition to potentially controlling the arc behavior and ultimately reducing its impact on the quality of the final ingot.

Author Contributions: Conceptualization, A.J., P.C. and P.-O.D.; methodology, A.J., P.C. and P.-O.D.; software, A.M.; formal analysis, A.J., P.C., P.-O.D. and A.M.; investigation, P.-O.D. and A.M.; writing—original draft preparation, P.C. and A.J.; writing—review and editing, P.C., A.J., P.-O.D., A.M. and Y.M. All authors have read and agreed to the published version of the manuscript.

Funding: This research work was partially supported by the French Ministry for Research and Education through a CIFRE contract with TIMET Savoie company (Convention CIFRE N° 2014/0721).

Institutional Review Board Statement: Not applicable.

Informed Consent Statement: Not applicable.

Data Availability Statement: Data sharing not applicable.

Conflicts of Interest: The authors declare no conflict of interest. The funders had no role in the design of the study; in the collection, analyses, or interpretation of data; in the writing of the manuscript, or in the decision to publish the results.

References

1. Delzant, P.-O.; Chapelle, P.; Jardy, A.; Jourdan, J.; Jourdan, J.; Millet, Y. Investigation of arc dynamics during vacuum arc remelting of a Ti64 alloy using a photodiode based instrumentation. *J. Mater. Process. Technol.* **2019**, *266*, 10–18. [CrossRef]
2. Shevchenko, D.M.; Ward, R.M. Liquid metal flow behaviour during the VAR of Inconel 718. In Proceedings of the 2007 International Symposium on Liquid Metal Processing and Casting: LMPC 2007, Nancy, France, 2–5 September 2007; p. 25.
3. Zanner, F.J. Observation of the vacuum arc and metal transfer during vacuum consumable arc remelting. In Proceedings of the Sixth International Vacuum Metallurgy Conference on Special Melting, San Diego, CA, USA, 23–27 April 1979; Bhat, G.K., Schlatter, R., Eds.; American Vacuum Society: New York, NY, USA, 1979; pp. 417–427.
4. Chapelle, P.; Bellot, J.-P.; Jardy, A.; Czerwiec, T.; Robbe, X.; Champin, B.; Ablitzer, D. An experimental study of the electric arc during vacuum arc remelting. *High Temp. Mater. Process.* **2000**, *4*, 493–506. [CrossRef]
5. Chapelle, P.; Noël, C.; Risacher, A.; Jourdan, J.; Jardy, A.; Jourdan, J. Optical investigation of the behavior of the electric arc and the metal transfer during vacuum remelting of a Ti alloy. *J. Mater. Process. Technol.* **2014**, *214*, 2268–2275. [CrossRef]
6. Zanner, F.J.; Bertram, L.A. Vacuum arc remelting: An overview. In Proceedings of the 8th International Conference On Vacuum Metallurgy, Linz, Austria, 30 September–4 October 1985; Volume 1, pp. 512–552.
7. Ward, R.M.; Daniel, B.; Siddall, R.J. Ensemble arc motion and solidification during the vacuum arc remelting of a nickel based superalloy. In Proceedings of the International Symposium on Liquid Metal Processing and Casting, Santa Fe, NM, USA, 18–21 September 2005; pp. 49–56.

8. Woodside, C.R.; King, P.E.; Nordlund, C. Arc distribution during the vacuum arc remelting of Ti-6Al-4V. *Metall. Mater. Trans. B* **2013**, *44*, 154–165. [CrossRef]
9. Aikin, R.M.; Williamson, R.L. A new optical emission monitor for vacuum arc remelting. In Proceedings of the International Symposium on Liquid Metal Processing and Casting, Santa Fe, NM, USA, 20–23 September 2009; pp. 65–74.
10. Bertram, L.A.; Adasczik, C.B.; Evans, D.G.; Minisandram, P.A.; Wegman, D.D.; Williamson, R.L. Quantitative simulations of a superalloy VAR ingot at the macroscale. In Proceedings of the Vacuum Metallurgy Conference on Liquid Metal Processing and Casting, Santa Fe, NM, USA, 16–19 February 1997; pp. 110–132.
11. Xu, X.; Zhang, W.; Lee, P.D. Tree-ring formation during vacuum arc remelting of INCONEL 718: Part II. Mathematical modeling. *Metall. Mater. Trans. A* **2002**, *33*, 1805–1815. [CrossRef]
12. Jardy, A.; Ablitzer, D. Solar: Numerical software to optimize vacuum arc remelting operation. *Rare Met. Mater. Eng.* **2006**, *35*, 119–122.
13. Yuan, L.; Djambazov, G.; Lee, P.D.; Pericleous, K. Multiscale modeling of the vacuum arc remelting process for the prediction on microstructure formation. *Int. J. Mod. Phys. B* **2009**, *23*, 1584–1590. [CrossRef]
14. Pericleous, K.; Djambazov, G.; Ward, M.; Yuan, L.; Lee, P.D. A multiscale 3D model of the vacuum arc remelting process. *Metall. Mater. Trans. A* **2013**, *44*, 5365–5376. [CrossRef]
15. Spitans, S.; Franz, H.; Scholz, H.; Reiter, G.; Baake, E. Numerical simulation of the ingot growth during the vacuum arc remelting process. *Magnetohydrodynamics* **2017**, *53*, 553–569.
16. Karimi-Sibaki, E.; Kharicha, A.; Abdi, M.; Vakhrushev, A.; Wu, M.; Ludwig, A.; Bohacek, J. A numerical study on the influence of an axial magnetic field (AMF) on vacuum arc remelting (VAR) process. *Metall. Mater. Trans.* **2021**, *52*, 3354–3362. [CrossRef]
17. Nair, B.G.; Jourdan, J.; Millet, Y.; Ward, R.M. The influence of magnetic stirring on the measured arc behavior during VAR of a near alpha-Ti alloy. In Proceedings of the International Symposium on Liquid Metal Processing and Casting, Santa Fe, NM, USA, 10–13 September 2017; pp. 15–20.
18. Jardy, A.; Hans, S. Use of numerical modelling to study the impact of operating parameters on the quality of a vacuum arc remelted ingot. In Proceedings of the 11th International Conference on Modeling of Casting, Welding and Advanced Solidification Processes, Opio, France, 28 May–2 June 2006; pp. 953–996.
19. Wilson, A.F.; Jardy, A.; Fox, S.P. A numerical study of the influence of stirring parameters on titanium ingot quality using SOLAR V4.2. In Proceedings of the 11th World Conference on Titanium, Kyoto, Japan, 3–7 June 2007; pp. 869–872.
20. Revil-Baudard, M.; Jardy, A.; Combeau, H.; Leclerc, F.; Rebeyrolle, V. Solidification of a vacuum arc remelted zirconium ingot. *Metall. Mater. Trans. B* **2014**, *45*, 51–57. [CrossRef]
21. Matveichev, A.; Jardy, A.; Bellot, J.-P. A full 3D model of fluid flow and heat transfer in an E.B. heated liquid metal bath. *IOP Conf. Ser. Mater. Sci. Eng.* **2016**, *143*, 012019. [CrossRef]
22. Weller, H.G.; Tabor, G.; Jasak, H.; Fureby, C. A tensorial approach to computational continuum mechanics using object-oriented techniques. *Comput. Phys.* **1998**, *12*, 620–631. [CrossRef]
23. Valencia, J.J.; Quested, P.N. Thermophysical properties. *ASM Handb.* **2008**, *15*, 468–481.
24. Boivineau, M.; Cagran, C.; Doytier, D.; Eyraud, V.; Nadal, M.-H.; Wilthan, B.; Pottlacher, G. Thermophysical properties of solid and liquid Ti-6Al-4V (TA6V) alloy. *Int. J. Thermophys.* **2006**, *27*, 507–529. [CrossRef]